

Synthesis of Co-doped ZnO nanoparticles by sol–gel method and its characterization

J. El Ghoul · M. Kraini · L. El Mir

Received: 1 December 2014 / Accepted: 17 January 2015 / Published online: 7 February 2015
© Springer Science+Business Media New York 2015

Abstract Cobalt doped ZnO nanoparticles with different Co contents have been synthesized by a sol–gel processing technique. In our approach, the water for hydrolysis was slowly released by esterification reaction followed by a supercritical drying in ethyl alcohol. The structural, morphological, optical and magnetic properties of the as-prepared nanoparticles were investigated by XRD, transmission electron microscopy, UV measurements, photoluminescence and superconducting quantum interference device. The structural properties showed that the obtained nanoparticles are in wurtzite single crystalline phase and no secondary phases were detected which indicated that Co substituted Zn ions. The energy band gap of the ZnO host matrix decreases gradually by increasing the doping concentration. The photoluminescence spectra exhibit intensive emission in the UV range. This emission presents a small shift to longer wavelengths and remarkable decreases in the intensity with increasing Co content. The Magnetic measurements at room temperature reveal diamagnetic behavior for the samples with lower doping concentrations; however, at higher Co content, we noted the presence of both paramagnetic and ferromagnetic behaviors.

1 Introduction

In recent years, semiconductor nanoparticles have attracted great interest [1–3]. This is stimulated mainly by physical probe into low-dimensional systems and potential applications for this class of materials. They always exhibit novel optical, electrical, and mechanical properties due to quantum confinement effects compared with their bulk counterparts, and thus can be applied in many areas, including luminescent devices, solar cells, chemical sensors, and biological labeling and diagnostics.

Due to its excellent optical, electrical, mechanical and chemical properties, ZnO semiconductor has attracted a great deal of attention in the material research field. Due to its significant optical and electronic properties, ZnO has been widely used for the fabrication of various nano-optoelectronic devices [4–7]. Recently, the doping by well-chosen impurities has been extensively explored as an effective technique to modify the ZnO nanostructures properties [8–12]. Metal transition (MT) elements doping ZnO has become an active research field ever since it was predicted to improve the optical and electronic properties of the material oxide, and particularly, lead to room-temperature ferromagnetism. Among them, the Co is considered as a potential candidate because of its abundant electron states and large solubility in the ZnO matrix [13]. Many groups have synthesized Co-doped ZnO nanostructures and studied the altered performance upon doping. For instance, Jones and coworkers [14] fabricated ZnO:Co submicrometer tubes using a polymer based template approach. They observed a 25-nm red shift in UV–vis absorption, which originated from the narrowing of the ZnO band gap (3.22 eV) as a result of Co doping. Wang's group [15] synthesized ZnO:Co nanorod arrays on a glass substrate via a solution route. They found that Co doping

J. El Ghoul (✉) · L. El Mir
Department of Physics, College of Sciences, Al Imam
Mohammad Ibn Saud Islamic University (IMSIU),
Riyadh 11623, Saudi Arabia
e-mail: jaber.elghoul@fsg.rnu.tn; ghoultn@yahoo.fr

J. El Ghoul · M. Kraini (✉) · L. El Mir
Laboratory of Physics of Materials and Nanomaterials Applied at
Environment (LaPhyMNE), Faculty of Sciences in Gabes, Gabes
University, 6072 Gabes, Tunisia
e-mail: mabrouk.karini@gmail.com

can effectively adjust the energy level in ZnO nanorods, lead to variation in the UV emission peak position, and enhance the luminescence performance in the visible region. Bahadur's group [16] synthesized uniform and transparent $\text{Zn}_{1-x}\text{Co}_x\text{O}$ films by a sol-gel spin coating technique, and revealed that an increase in Co content in the range $0 \leq x \leq 0.10$ led to a decrease in band gap energy as well as quenching of the near band edge and blue emissions. Sharma et al. [17] prepared ZnO:Co nanoparticles by a co-precipitation technique. The obtained samples showed strong ferromagnetic behavior at room temperature. However, at higher doping levels, the ferromagnetic behavior was suppressed and the antiferromagnetic nature was enhanced. Xu and Cao [18] reported a hydrothermal method to synthesis $\text{Zn}_{1-x}\text{Co}_x\text{O}$ flakes, and found that the samples exhibited obvious ferromagnetic characteristics at room temperature. Moreover, with more doping content of Co^{2+} , the ferromagnetic behavior was suppressed and paramagnetic nature was observed. Previous studies have obviously demonstrated that the physical and chemical properties of the synthesized $\text{Zn}_{1-x}\text{Co}_x\text{O}$ samples are strongly sensitive to its preparative conditions [15, 16]. Over the past few years, much efforts have been made to investigate wet chemical methods for the synthesis of metal-ion-doped ZnO nanostructures, including the sol-gel method [19, 20] and various hydrothermal methods [21, 22]. Motivated by these reasons, we report in this paper a new approach to obtain such powders based on hydrolysis of zinc acetate in methanol followed by supercritical drying in ethanol using modified sol-gel process. The effect of cobalt as metal transition doping element on structural, optical and magnetic properties of the powder is investigated for different concentrations.

2 Experimental

Cobalt-doped ZnO nanocrystals were prepared by the sol-gel method using 16 g of zinc acetate dehydrate as precursor in a 112 ml of methanol. After magnetic stirring at room temperature, the appropriate amount of cobalt acetate was added, and the solution was placed in an autoclave and dried under supercritical conditions of ethyl alcohol using our previous protocol [23–25].

X-ray diffraction (XRD) patterns of cobalt doped zinc oxide nanopowder were carried out by a Bruker D5005 diffractometer, using $\text{CuK}\alpha$ radiation ($\lambda = 1.5418 \text{ \AA}$).

Crystallite sizes (G , in \AA) were estimated from the Debye-Scherrer Eq. (1) [26]:

$$G = 0.9\lambda/B \cos \theta_B \quad (1)$$

where λ is the X-ray wavelength (1.5418 \AA), θ_B is the maximum of the Bragg diffraction peak and B is the line

width at half maximum. The synthesized products were also characterized using a JEM-200CX transmission electron microscopy (TEM). The dopant content and the chemical bonding states of the cobalt ions in the $\text{Zn}_{1-x}\text{Co}_x\text{O}$ nanocrystallites were determined by EDX analysis. The specimens for TEM were prepared by putting the as-grown products in EtOH and immersing them in an ultrasonic bath for 15 min, then dropping a few drops of the resulting suspension containing the synthesized materials onto TEM grid. Room-temperature optical spectra in the UV-visible range were collected using a Shimadzu UV-3101 PC spectrophotometer fitted with an integrating sphere diffuse reflectance accessory. The spectrophotometer measures reflectance relative to a background scatterer, which was powdered BaSO_4 . For PL measurements, the 337.1 nm laser line of a Laser Photonics LN 100 nitrogen laser was used as an excitation source. The emitted light from the sample, collected by an optical fiber on the same side as the excitation, was analyzed by a Jobin-Yvon Spectrometer HR460 and a multichannel CCD detector (2,000 pixels). Magnetic analysis were carried out at different measurement temperatures between 2 and 400 K and in the magnetic field range from -60 to $+60$ kOe, using a commercial superconducting quantum interference device (SQUID) magnetometer (Quantum Design, MPMS XL).

3 Results and discussion

Figure 1 shows the XRD patterns of $\text{Zn}_{1-x}\text{Co}_x\text{O}$ ($0.00 \leq x \leq 0.05$) samples, which were indexed using POWDER-X software as the ZnO wurtzite structure and well matched with the standard data (JCPDS, 36-1451). It

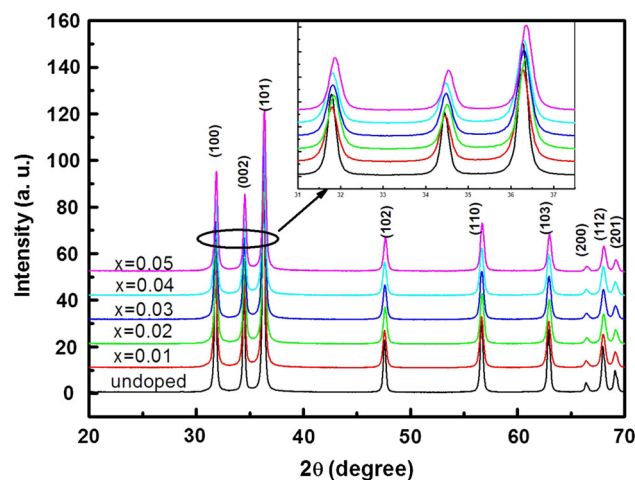


Fig. 1 XRD patterns of $\text{Zn}_{1-x}\text{Co}_x\text{O}$ nanoparticles. The inset displays the shifting and broadening of (100), (0 0 2) and (1 0 1) peaks for increasing Co content

can be clearly seen from the XRD patterns that all the samples showed a single phase nature with hexagonal wurtzite structure [26]. No secondary phase was detected and this indicates that the Co dopant is incorporated into the lattice as a substitutional atom. We can notice also that the peaks are very broad which indicates the formation of very fine particles in the nanoscale range. The average crystallite size obtained using Debye-Scherrer formula confirmed this result. Table 1 summarizes the lattices parameters obtained from XRD for several concentrations. It can be seen that the lattice parameter *c* values of Zn_{1-x}Co_xO are smaller than the value of undoped ZnO (*c* = 5.208), which is close to the standard value (ICSD reference number: 67848-1993 (5.212 Å) and 67454-1989 (5.207 Å)). We observed a decrease in the lattice constant value with increasing concentration of Co ions. This decrease of lattice constant with Co contents is corroborated by the shift of the peaks position (in-set in Fig. 1). Moreover, with increasing the Co doping content, we also found that the intensity of the diffraction peak decreased gradually and the width broadened, which might be due to the increase in the lattice disorder and strain induced by Co²⁺ substitution. The decrease of lattice parameters can be explained by the fact that the effective ionic radius of Co²⁺ in tetrahedral configuration (0.58 Å) is smaller than that of Zn²⁺ (0.60 Å) ions [27]. This reduction in lattice parameters may be also due to the decrease of the nanoparticles size after doping [28]. In addition, for *x* = 0.05, we observed an increase of the lattice parameters which can be explained by the incorporation of Co³⁺ ions with significant lattice defects [29].

The average grain size was calculated from Scherrer’s formula (1) using the most intense peak (101). The values summarized in Table 1 show that the grain size decreases with increasing Co concentration.

Figure 2a–d shows the TEM images for the different samples of Zn_{1-x}Co_xO (*x* = 0.0, 0.01, 0.03 and 0.05). It can be seen that the samples are nearly spherical with the diameters ranging from 18 to 30 nm. It can also be noticed from these images that the average particle decreases with increasing Co concentration, which is in agreement with XRD results. HRTEM image (Fig. 2e) showed that the measured distance between the planes is around 0.260 nm,

which is corresponding to the (002) planes of the wurtzite ZnO. The EDX spectra of the doped samples are shown in Fig. 2g–h. Zn and O appeared as the main components with low levels of Co. An increase in the relative intensities of the Co peaks with the increasing of the dopant concentration was also observed, confirming the progressive incorporation of Co. This ensures the uniform distribution of the doped Co ions as expected in the chemical synthesis process employed in this work.

The absorption properties of ZnO nanoparticles after doping were also investigated. UV–visible diffuse reflectance spectroscopy (UV/DRS) was initially used to study the band gap of ZnO nanocrystallites. Figure 3 presents the typical absorption spectra of the samples doped with different concentrations. In the case of Co-doped nanorods, three extra absorption bands have been observed at 655, 615 and 565 nm (see Fig. 3). Based on the optical studies performed of Co-doped ZnO single crystals [30], these edges are assigned to the d–d crystal-field transitions ⁴A₂(F) → ²E(G), ⁴A₂(F) → ⁴T₁(P) and ⁴A₂(F) → ²T₁(G). The appearance of these transitions clearly suggests that the Co²⁺ is in the high-spin (*S* = 3/2) state and are under a tetrahedral crystal field, in agreement with similar studies on Zn_{1-x}Co_xO thin films [31]. Wurtzite ZnO has Zn²⁺ ions in tetrahedral sites [32] and therefore Co²⁺ ions seem to substitute the Zn²⁺ ions in this lattice.

Optical diffuse reflectance spectra of undoped and doped ZnO nanorods, measured at room temperature, are shown in Fig. 4. The reflectance spectral data were converted to the Kubelka–Munk function, *F*(*R*) by applying the equation:

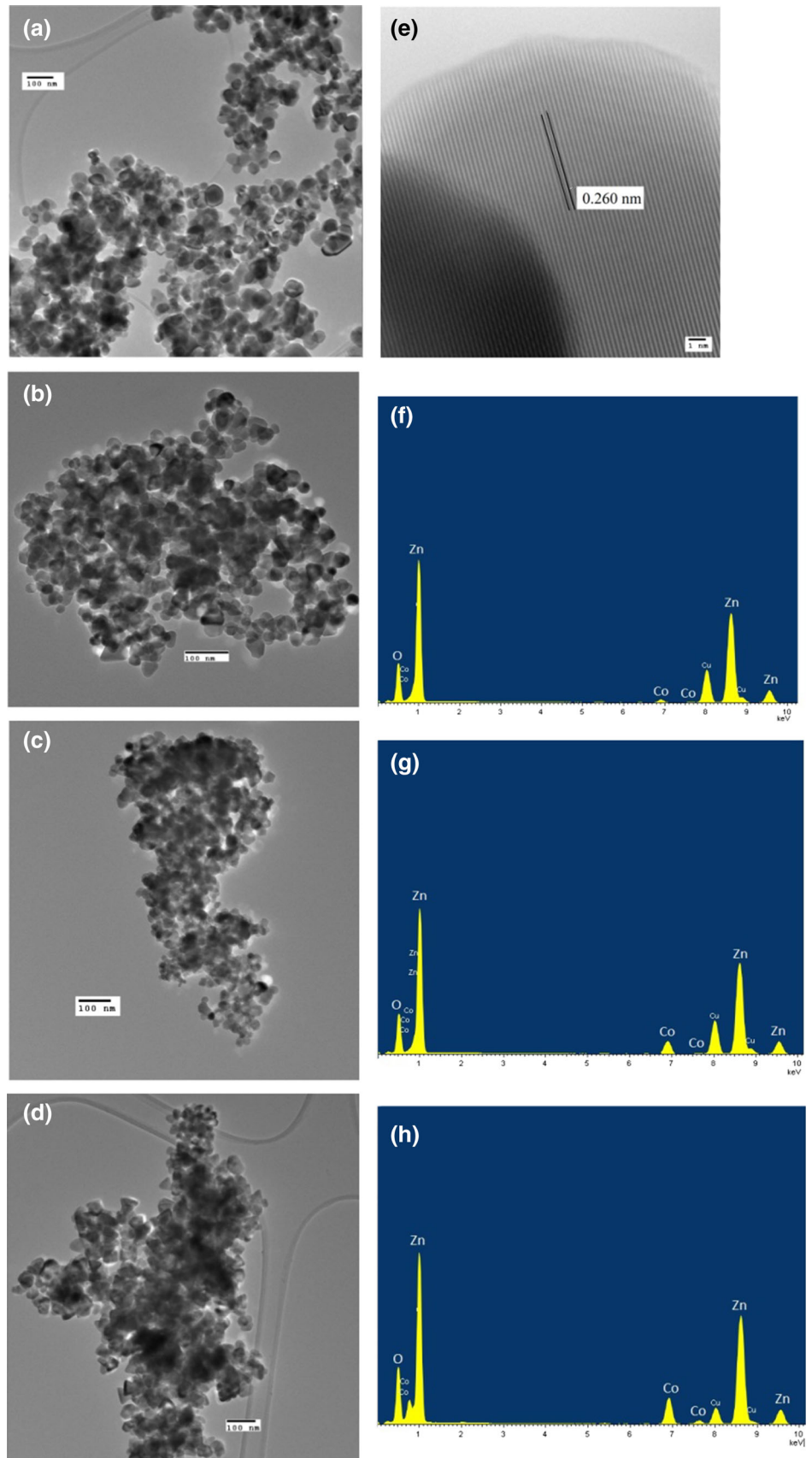
$$F(R) = \frac{(1 - R)^2}{2R} \tag{2}$$

The direct band gap (*E*_g) energies of the Zn_{1-x}Co_xO powders were calculated from their diffuse-reflectance spectra by plotting [*F*(*R*).*hν*]^{*n*} versus *hν*. A direct band gap semiconductor gives a linear Tauc region just above the optical absorption edge with *n* = 2, whilst an indirect semiconductor gives a linear region with *n* = 0.5 [33]. A direct band gap semiconductor was assumed for these samples since a linear region just above the gap edges was observed with *n* = 2. The linear part of the curve was

Table 1 Co doping concentration dependency of the average size, lattice constant *c* and band gap energies of Zn_{1-x}Co_xO nanoparticles

Concentration of Co (%)	Average size (nm)	Lattice parameter <i>c</i> (Å°)	Energy (eV)
0	28	5.208	3.335
1	27	5.204	3.135
2	23	5.197	3.087
3	21	5.192	3.021
4	20	5.191	2.993
5	19	5.196	2.972

Fig. 2 HR-TEM images and EDX analysis of (a) ZnO, (b) $\text{Zn}_{0.99}\text{Co}_{0.01}\text{O}$, (c) $\text{Zn}_{0.97}\text{Co}_{0.03}\text{O}$, and (d) $\text{Zn}_{0.95}\text{Co}_{0.05}\text{O}$ nanoparticles



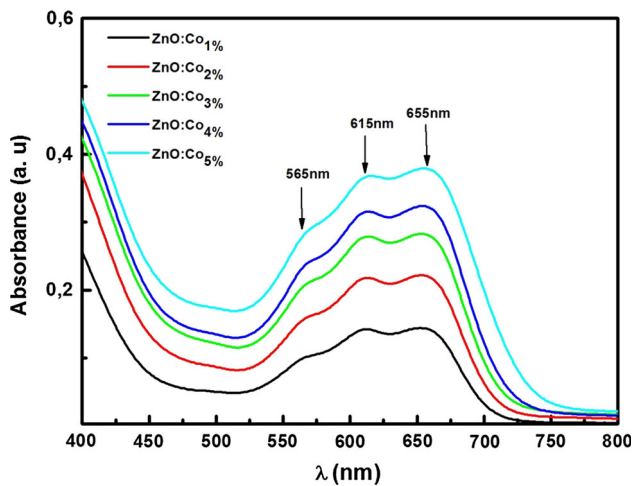


Fig. 3 Room-temperature absorbance spectra of $Zn_{1-x}Co_xO$ samples

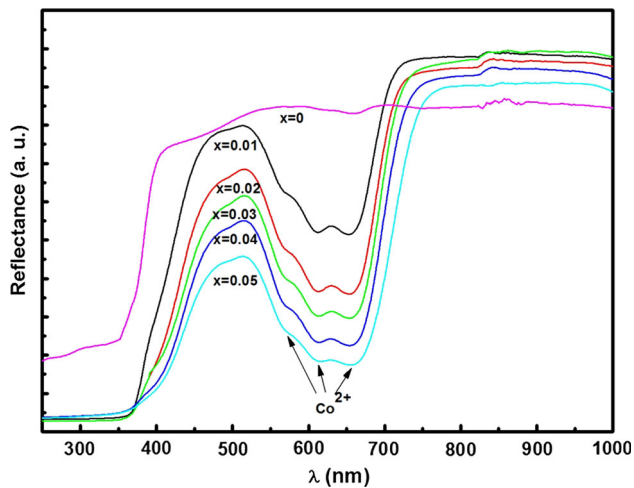


Fig. 4 Room-temperature diffuse reflectance spectra of $Zn_{1-x}Co_xO$ samples

extrapolated to $[F(R) \cdot hv]^2 = 0$ in order to estimate the direct band gap energy shown in Fig. 5; the in-set shows that the values of the E_g of the $ZnO:Co$ samples decrease with increasing x . A similar decrease in the band gap energy with Co concentration has been reported by Kim and Park [29], although an opposite behaviour was observed by Schwartz et al. [34] in $Zn_{1-x}Co_xO$ nanocrystals. Kim and Park [29] have argued that the band gap narrowing with increasing x is due to the $sp-d$ exchange interactions between the band electrons and the localized d electrons of the substituted Co^{2+} ions. Ando et al. [35] reported that the magneto-optical effect in $Zn_{1-x}Co_xO$ is the largest observed between different transition metal dopants used indicating a strong exchange interaction between the electrons of the strip and sp of localized electrons, supporting this possibility.

Figure 6 shows the room temperature photoluminescence spectra under 325 nm excitation wavelength of all

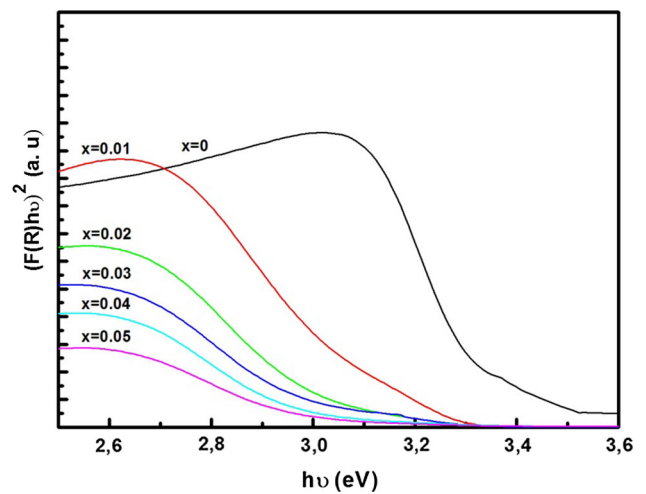


Fig. 5 Plot $[F(R) \cdot hv]^2$ versus photon energy ($h\nu$). The in-set showing the variation of the band gap energy with x

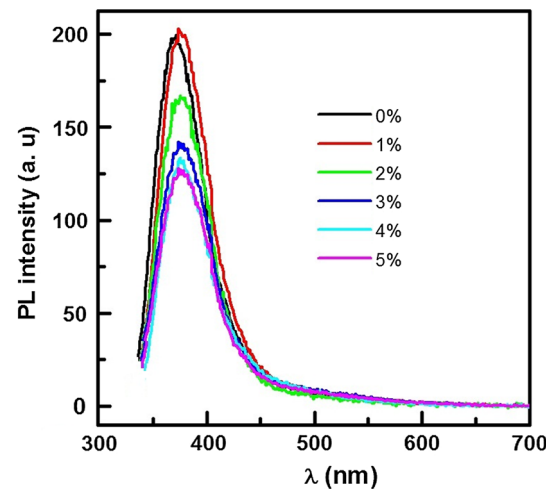


Fig. 6 Room temperature photoluminescence spectra of $Zn_{1-x}Co_xO$ samples

samples. There are many works that report similar studies; they have shown the presence of UV emission with different behaviors depending on Co content. For example, some reports have revealed that Co-doped ZnO alloys show the red-shift of E_g for Co-doped ZnO nanorods [36, 37], while blue-shift phenomena have been also observed in Co-doped ZnO films [38] and epilayers [39]. The weak ultraviolet (UV) emission is assigned to the band-edge exciton of ZnO. Compared with ZnO sample, the peak position of the UV emission shifts to shorter wavelengths with increasing Co content, which indicates that the band-gap of the ZnO nanowires can be adjusted by the doping with Co. It was suggested that the peak position of UV emission in Co doped ZnO nanowires is affected by Burstein-Moss effect and defects in the crystal. The peak shifts to short wavelength because of Burstein-Moss effect, while

the defects in the crystals result in the emission peak shift to long wavelength. In our works, the peak positions for ZnO:Co samples slightly shift to the longer wavelength in comparison with the pure ZnO. This is due to the band gap narrowing of the ZnO nanocrystals with Co incorporation, as discussed in the previous section.

As the impurity effects dominate the photoluminescence from pure materials and the exciton moves through the materials, it encounters defects, and the exciton tends to decay in the vicinity of these centers. Under the same excitation condition, the intensity of the UV emission decreases with increasing Co, which suggests that the crystal quality is decreased by the doping with Co. As the diameter of the Co^{2+} ions is different from that of Zn^{2+} , more Co^{2+} ions substitute Zn^{2+} , more stress are induced in the materials, and the crystal quality is destroyed in some degree. Antony et al. [40] also found that the UV emission disappeared in the Co doped ZnO nanoclusters.

The magnetic properties of these powders were measured at room temperature (300 K). Figure 7a shows the dependence of magnetization on the applied magnetic field (M–H

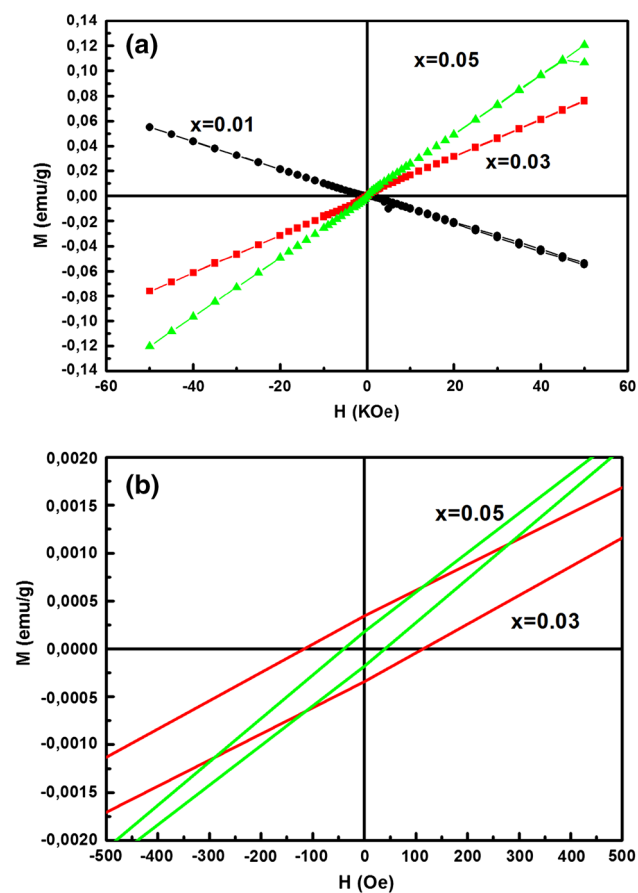


Fig. 7 Magnetization curve of (a) $\text{Zn}_{1-x}\text{Co}_x\text{O}$ ($x = 0.00, 0.01, 0.03$ and 0.05) at room temperature and (b) the magnified loop of $\text{Zn}_{1-x}\text{Co}_x\text{O}$ ($x = 0.03$ and 0.05)

curves). For $\text{Zn}_{1-x}\text{Co}_x\text{O}$ ($x = 0.01$) sample, we observe a diamagnetic behaviour similar to that obtained in general for undoped ZnO. For higher concentrations ($x = 0.03$ and 0.05), magnetization curves show that the samples have both paramagnetic and ferromagnetic behavior. At lower field, we observed a weak ferromagnetic component and paramagnetic component at higher field values. The hysteresis loops for $\text{Zn}_{1-x}\text{Co}_x\text{O}$ ($x = 0.03$ and 0.05) samples shown in Fig. 7b present with the coercivity (H_c) values of 117 and 43 Oe and the remnant magnetization (M_r) values of 3.52×10^{-4} and 1.5×10^{-4} emu/g, respectively. Regarding the origin of the ferromagnetic in our samples; there are several mechanisms that can induce in general to this phenomenon. For example, the lattice defects and the secondary phases could be the origin of ferromagnetism ordering in this kind of systems. In our case, XRD shows that the lattice parameters increase with Co concentration which can affect the crystal quality. The presence of secondary phase of Co metal clusters has been ruled out by our XRD results. The ferromagnetism behavior could be also explained by the ferromagnetic coupling between substituting Co in the ZnO host material [41]. Another mechanism related to the concept of bound magnetic polarons (BMPs) in connection with magnetic semiconductors can be introduced here to explain the origin of the ferromagnetism in our system [42, 43]. In the current experiment, the doping of Co impurity produced a number of oxygen vacancies and/or interstitial zinc that may act as shallow donor electrons and form BMPs. The overlapping of the polarons created a spin-split impurity band, which can mediate the Co–Co coupling in a ferromagnetism way, and thus, resulted in the ferromagnetic behavior of the sample. As Co dopant content increase, more probable for the doped Co^{2+} cations to occupy the next nearest lattice sites. The nearest Co–Co pairs then coupled in an antiferromagnetic way [17] and suppressed the magnetization [44]. This interpretation can explain the decrease in saturation for sample with $x = 0.05$ (3.52×10^{-4} emu/g) compared to the value obtained for $x = 0.03$ (1.5×10^{-4} emu/g). We can conclude that the room temperature ferromagnetism in our samples could be related to the defects and/or the coupling between substituting Co in the ZnO host matrix. Therefore, more studies have to be done to understand the room-temperature ferromagnetism in transition metal-doped ZnO.

Figure 8 shows the magnetization as a function of measurement temperature (T). The behaviors are discussed based on a simple molecular field theory. First, the magnetization of undoped and the $\text{Zn}_{1-x}\text{Co}_x\text{O}$ ($x = 0.01$) samples show a diamagnetic behavior. The samples $x = 0.03$ and 0.05 show no ferromagnetic transition in the temperature range 10–300 K. The magnetization increases with decreasing temperature and a rapid increase occurs at low temperature (25 K), this behavior is similar to paramagnetic one. However, the non-zero remnant

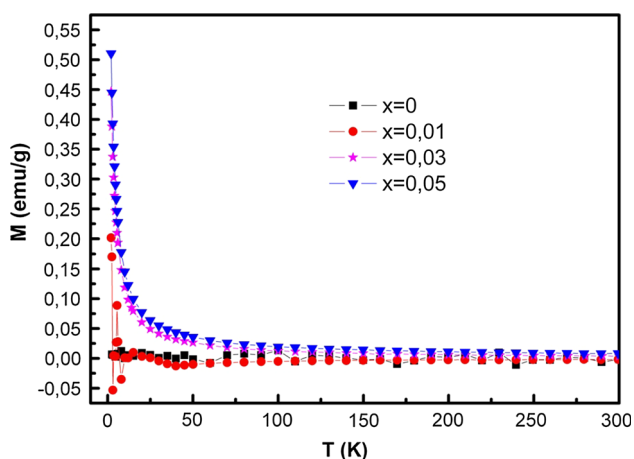


Fig. 8 Magnetization of $\text{Zn}_{1-x}\text{Co}_x\text{O}$ ($x = 0.00, 0.01, 0.03$ and 0.05) as a function of temperature

magnetization at room temperature and rapid increase of magnetization at very low temperature indicate the existence of FM. These results are in good agreement with (M-H) measurements.

4 Conclusion

Zinc oxide nanocrystallites with different cobalt doping loadings were successfully synthesized by a simple sol-gel method. The synthesis protocol is based on a slow hydrolysis of the precursor using an esterification reaction, followed by a supercritical drying in EtOH. XRD results indicated that all the synthesized un-doped and Co doped ZnO samples had a wurtzite structure and no secondary phases were detected which indicated that Co ions substituted the Zn. TEM results revealed that the prepared Co doped ZnO nanoparticles are nearly spherical in shape with particle size <30 nm, which is in good agreement with the sizes obtained by XRD. The band gap energy of the samples decreases from 3.33 eV for undoped ZnO to 2.97 eV for ZnO:Co 5 at.%, indicating that Co doping has a crucial influence on the energy band of the ZnO. Furthermore, the $\text{Zn}_{1-x}\text{Co}_x\text{O}$ samples exhibit diamagnetic characteristics for $x = 0.01$ and weak ferromagnetic with more doping content of Co^{2+} , the ferromagnetic behavior is suppressed and paramagnetic nature is observed at higher field values.

References

1. A.P. Alivisatos, *Science* **271**, 933–937 (1996)
2. D.J. Norris, N. Yao, F.T. Charnock, T.A. Kennedy, *Nano Lett.* **1**, 429–433 (2001)
3. M. Nirmal, L. Brus, *Acc. Chem. Res.* **32**, 407–414 (1999)

4. H.M. Yang, S. Nie, *Mater. Chem. Phys.* **114**, 279–282 (2009)
5. M. Yang, Z.X. Guo, K.H. Qiu, J.P. Long, G.F. Yin, D.G. Guan, S.T. Liu, S.J. Zhou, *Appl. Surf. Sci.* **256**, 4201–4205 (2010)
6. S.S. Lin, J.H. Song, Y.F. Lu, Z.L. Wang, *Nanotechnology* **20**, 365703 (2009)
7. M. Krunks, A. Katerski, T. Dedova, I.O. Acik, A. Mere, *Sol. Energy Mater. Sol. Cells* **92**, 1016–1019 (2008)
8. S. Rasouli, S.J. Moeen, *J. Alloys Compd.* **509**, 1915–1919 (2011)
9. J.B. Cui, Y.C. Soo, T.P. Chen, *J. Phys. Chem. C* **112**, 4475–4479 (2008)
10. Z. Sofer, D. Sedmidubský, S. Huber, J. Hejtmánek, M. Maryško, K. Jurek, M. Mikulics, *J. Cryst. Growth* **314**, 123–128 (2011)
11. X.R. Qu, D.C. Jia, *Mater. Lett.* **63**, 412–414 (2009)
12. Q. Chen, J.L. Wang, *Chem. Phys. Lett.* **474**, 336–341 (2009)
13. H.B. Carvalho, M.P.F. Godoy, R.W.D. Paes, M. Mir, A.O. Zavallos, F. Iikawa, M.J.S.P. Brasil, V.A. Chitta, W.B. Ferraz, M.A. Boselli, A.C.S. Sabioni, *J. Appl. Phys.* **108**, 033914 (2010)
14. F. Ochanda, K. Cho, D. Andala, T.C. Keane, A. Atkinson, W.E. Jones, *Langmuir* **25**, 7547–7552 (2009)
15. B.Q. Wang, X.D. Shan, Q. Fu, J. Iqbal, Y. Lv, H.G. Fu, D.P. Yu, *Phys. E* **41**, 413–417 (2009)
16. N. Bahadur, A.K. Srivastava, S. Kumar, M. Deepa, B. Nag, *Thin Solid Films* **518**, 5257–5264 (2010)
17. P.K. Sharma, R.K. Dutta, A.C. Pandey, *J. Colloid, Interface Sci.* **345**, 149–153 (2010)
18. X.Y. Xu, C.B. Cao, *J. Alloys Compd.* **501**, 265–268 (2010)
19. J.H. Yang, L.Y. Zhao, X. Ding, L.L. Yang, Y.J. Zhang, Y.X. Wang, H.L. Liu, *Mater. Sci. Eng. B* **162**, 143–146 (2009)
20. M.E. Mercurio, A.W. Carbonari, M.R. Cordeiro, R.N. Saxena, L.Z. D'Agostino, *J. Magn. Magn. Mater.* **322**, 1195–1197 (2010)
21. X.L. Zhang, R. Qiao, J.C. Kim, Y.S. Kang, *Cryst. Growth Des.* **8**, 2609–2613 (2008)
22. A. Singhal, S.N. Achary, J. Manjanna, S. Chatterjee, P. Ayyub, A.K. Tyagi, *J. Phys. Chem. C* **114**, 3422–3430 (2010)
23. L. El Mir, A. Amlouk, C. Barthou, S. Alaya, *J. Phys. B* **388**, 412–417 (2007)
24. L. El Mir, Z. Ben Ayadi, M. Saadoun, H. Von Bardeleben, K. Djessas, A. Zeinert, *Phys. Status Solidi* **204**, 3266–3277 (2007)
25. L. El Mir, Z. Ben Ayadi, H. Rahmouni, J. El Ghoul, K. Djessas, H.J. von Bardeleben, *Thin Solid Films* **517**, 6007–6011 (2009)
26. J. El Ghoul, C. Barthou, L. El Mir, *Superlattices Microstruct.* **51**, 942–951 (2012)
27. L.W. Yang, X.L. Wu, T. Qiu, G.G. Siu, P.K. Chu, *J. Appl. Phys.* **99**, 074303–074307 (2006)
28. J. El Ghoul, C. Barthou, L. El Mir, *Physica E* **44**, 1910–1915 (2012)
29. K.J. Kim, Y.R. Park, *Appl. Phys. Lett.* **81**, 1420–1422 (2002)
30. D.K. Sardar, J.B. Gruber, B. Zandi, M. Ferry, M.R. Kokta, *J. Appl. Phys.* **91**, 4846–4852 (2002)
31. S. Ramachandran, A. Tiwari, J. Narayan, *Appl. Phys. Lett.* **84**, 5255–5257 (2004)
32. A. Fouchet, W. Prellier, P. Padhan, Ch. Simon, B. Mercey, V.N. Kulkarni, T. Venkatesan, *J. Appl. Phys.* **95**, 7187–7189 (2004)
33. A.T. Kuvarega, R.W.M. Krause, B.B. Mamba, *J. Phys. Chem. C* **115**, 22110–22120 (2011)
34. D.A. Schwartz, N.S. Norberg, Q.P. Nguyen, J.M. Parker, D.R. Gamelin, *J. Am. Chem. Soc.* **125**, 13205–13218 (2003)
35. K. Ando, H. Saito, Z. Jin, T. Fukumura, M. Kawasaki, Y. Matsumoto, H. Koinuma, *J. Appl. Phys.* **89**, 7284–7286 (2001)
36. K.J. Kim, Y.R. Park, *Appl. Phys. Lett.* **81**, 1420–1422 (2002)
37. Y.J. Li, C.Y. Wang, M.Y. Lu, K.M. Li, L.J. Chen, *Cryst. Growth Des.* **8**, 2598–2602 (2008)
38. J.H. Kim, H. Kim, D. Kim, S.G. Yoon, W.K. Choo, *Solid State Commun.* **131**, 677–680 (2004)
39. W. Pacuski, D. Ferrand, J. Cibert, C. Deparis, J.A. Gaj, P. Koszacki, C. Morhain, *Phys. Rev. B* **73**, 035214–035226 (2006)

40. J. Antony, S. Pendyala, A. Sharma, X.B. Chen, J. Morrison, L. Bergman, Y. Qiang, *J. Appl. Phys.* **97**, 10D307-1 (2005)
41. S. Yang, Y. Zhang, *J. Magn. Magn. Mater.* **334**, 52–58 (2013)
42. R. Janisch, P. Gopal, N.A. Spaldin, *J. Phys. Condens. Matter* **17**, R657–R689 (2005)
43. J.M.D. Coey, M. Venkatesan, C.B. Fitzgerald, *Nat. Mater.* **4**, 173–179 (2005)
44. T. Büsgen, M. Hilgendorff, S. Irsen, F. Wilhelm, A. Rogalev, D. Goll, M. Giersig, *J. Phys. Chem. C* **112**, 2412–2417 (2008)